Combined electrochemical, heat generation, and thermal model for large prismatic lithium-ion batteries in real-time applications

Mohammed Farag [a, *, 1], Haitham Sweity [b, c], Matthias Fleckenstein [c], Saeid Habibi [a]

[a] McMaster University, Department of Mechanical Engineering, Center of Mechatronics and Hybrid Technologies CMHT, L8S4L8 Ontario, Canada
[b] Institute for Electrical Energy Storage Technology, Technische Universitaet Muenchen, Arcisstrae 21, 80333 Munich, Germany
[c] BMW Group, Battery Technology, 80788 Munich, Germany

HIGHLIGHTS

- A simplified combined electrochemical, heat generation and thermal model is proposed.
- Heat generation model that accounts for different loss mechanisms is developed.
- A real-time thermal model of a large format prismatic cells is proposed.
- Model parameterization under isothermal and non-isothermal operating conditions.
- Model validation using experimental data for broad C-rates, and temperature ranges.

ARTICLE INFO

ABSTRACT

Real-time prediction of the battery's core temperature and terminal voltage is very crucial for an accurate battery management system. In this paper, a combined electrochemical, heat generation, and thermal model is developed for large prismatic cells. The proposed model consists of three sub-models, an electrochemical model, heat generation model, and thermal model which are coupled together in an iterative fashion through physicochemical temperature dependent parameters. The proposed parameterization cycles identify the sub-models' parameters separately by exciting the battery under isothermal and non-isothermal operating conditions. The proposed combined model structure shows accurate terminal voltage and core temperature prediction at various operating conditions while maintaining a simple mathematical structure, making it ideal for real-time BMS applications. Finally, the model is validated against both isothermal and non-isothermal drive cycles, covering a broad range of C-rates, and temperature ranges [−25 °C to 45 °C].

© 2017 Elsevier B.V. All rights reserved.

1. Introduction

In the past decade, lithium-ion batteries have gradually gained acceptance in the automotive sector as electric energy storage due to their high specific energy, low self-discharge rate, and non-memory effect. In order to efficiently integrate the lithium-ion batteries in electric vehicles (EV), different cell sizes have been introduced. Depending on the method of packing, the cells can be shaped into a pouch, cylindrical, or prismatic form. Prismatic lithium-ion batteries have become one of the most attractive options for energy storage systems due to their optimal use of space and light weight. However, abnormal operating conditions such as over discharge, overcharge, or high operating temperature can accelerate their aging and degradation and may lead to thermal runaways in extreme cases. To fully benefit from a lithium-ion energy storage system and avoid its physical degradation, an accurate battery management system (BMS) is required. The BMS is responsible for the battery state of charge (SOC), state of health (SOH), state of power (SOP), and thermal management. It uses state estimation algorithms for monitoring, as well as operating the battery within a range that is considered as nominal in order to ensure safety and performance as well as preserving its projected useful life. One of the main requirements for a successful BMS implementation is the development of a high fidelity battery model

that includes thermal and aging dependent parameters. The battery model needs to be dynamically significant while being computationally efficient, robust, and accurate. Of particular interest is the prediction of the terminal voltage which is affected by the cell's core temperature. As such, an accurate thermal model is needed to predict the core temperature and estimate its dynamics. The inclusion of a thermal model within the overall battery model is necessary as it enables the BMS to operate the battery safely and preserve its performance effectively.

Battery models are broadly classified under three categories: equivalent circuit [1–4], behavioral (or black-box) [5–8], and electrochemical (physics-based) models [9–11]. The equivalent circuit models are widely used in BMS due to their acceptable accuracy, complexity, and fidelity. Most of the electrochemical modeling approaches found in the literature are based on the electrochemical pseudo-two-dimensional (P2D) model further developed following the Doyle-Fuller-Newman model [12,13]. The physics-based P2D model is very accurate; however, it is excessively computationally complex, thereby burdening its real-time implementation. Therefore, many model reduction methods have been proposed to reduce its complexity while maintaining its accuracy. The model reduction methods commonly used can be divided into two categories. One category focuses on reducing the computational complexity involved in solving the concentration of lithium in the solid particles of the electrodes by either simplifying the concentration profile or assuming it to be constant as presented by Refs. [14–16]. Another category focuses on reducing the electrochemical model as a whole, such as to avoid the solution of large sets of differential-algebraic equations (DAEs) of the Li^+ concentration distribution and the potential distribution of the electrolyte phase. Examples of the latter can be found in Refs. [17–19].

In order to investigate the dynamic behavior of the cell, two main approaches are discussed in the literature: (i) electrochemical impedance spectroscopy (EIS) and (ii) measurement of a voltage response using controlled input currents and then applying optimization techniques to determine the model parameters. The general principle of the EIS method is to apply an input signal either current (galvanostatic) or voltage (potentiostatic) and then measure the characteristic response of the cell which depends on the cell impedance. In the scope of this publication, the model is parameterized and validated using the second approach. The battery under test was subjected to charging, charge-sustaining and charge-depleting phases at six different temperature in order to determine the temperature dependency of the parameters. The genetic algorithm (GA) was then used to optimize the model parameters.

In addition, various strategies have been proposed in the literature for modeling the temperature profile inside a cell during its operation. These include coupled partial differential equations (PDE) models, linear parameter-varying state-space models, three-dimensional Finite Element Analysis (FEA) models and relatively simple lumped capacitance zero-dimensional thermal models. Smyshlyaev et al. [20] proposed an analytic solution for solving the thermal model PDEs. Whereas, Hu et al. [21] reduced the PDEs computational complexity by fitting a more complicated computational fluid dynamics (CFD) model to a linear parameter-varying state-space model. Guo et al. [22] presented a three-dimensional FEA thermal model, while Baba et al. [23] developed a full 3D thermal model that takes into account local heat generation and the spatial dependencies to obtain a full 3D temperature distribution of the cell. The FEA thermal models are very accurate; however, they require excessive computational power and specific material properties, which limit their real-time implementation especially when fluid dynamics are considered in the cooling process. Damay et al. [24] developed a lumped capacitance, zero-dimensional

thermal model. The model included one heat capacitor coupled with different modes of heat transfer throughout the cell to represent the thermal behavior of a prismatic cell. Similarly, Forgez et al. [25] employed the same technique for cylindrical cells using two heat capacitors. Further to the above, the lumped capacitance modeling approach will also be considered in this work due to its low computational complexity and acceptable accuracy. An accurate set of parameters is required for obtaining a high-fidelity thermal model. The thermal parameters are either determined analytically or experimentally. Lin et al. [26] used detailed information about the material and geometry of the cell for analytically determining the parameters. Perez et al. [27] used the least squares optimization algorithms to fit the model to the experimental data. Lin et al. [28] proposed an online estimation algorithm. Sastry et al. [29] developed a surrogate-based modeling and dimension reduction techniques to assess the role of design variables on multiple competing objectives for a wide range of engineering problems [30,31].

In this publication, an experimental method involving optimization will be used instead of the analytical methods as they suffer from a high level of uncertainty.

This paper proposes three unique contributions for improving battery modeling. The first contribution is a combined electrochemical, heat generation, and thermal model capable of accurately predicting the cell's terminal voltage and core temperature. The second contribution is an accurate yet computationally simple four-node thermal model (4NTM). The 4NTM helps in estimating the battery's core temperature leading to an increase in the terminal voltage accuracy within a broad range of temperatures [-25 °C–40 °C]. The four-node structure constitutes a reduced order form that renders the model suitable for real-time applications. The third contribution is a model parameterization scheme that allows identification of each sub-model parameters separately.

1.1. Paper structure

In section 2, the combined electrochemical, heat generation and thermal model is illustrated. Section 3, 4 and 5 presents the reduced-order electrochemical model (ROM), the heat generation model, and the thermal model respectively. In section 6, the parameter identification procedure and the experimental setup are explained. The ROM, 4NTM, and the combined ECHTM are then validated using battery voltage, current, and temperature measurements against different driving cycles. Finally, the conclusion, results, and future work are presented.

2. The combined model

This sections will present the main contribution of this paper, the formulation of a combined electrochemical, heat generation, and thermal model (ECHTM) that allows the BMS to effectively operate the battery in safe conditions and improve its terminal voltage, SOC, and SOH estimation accuracy. Fig. 1 shows a schematic representation of the combined ECHTM and its sub-models. The combined ECHTM is capable of estimating the cell's SOC, terminal voltage, and core temperature and it is divided into three different sub-models. First, the electrochemical model estimates the cells' terminal voltage V_t, SOC, open circuit potential $U_{p,n}$, and Li-ion concentration gradients $C_s^{n,p}$ as a function of the cell's core temperature T_c using physicochemical temperature dependent parameters. The cell's core temperature is calculated using a specific thermal model and fed back to the electrochemical model as an input. The heat losses are the most difficult elements to model due to the nonlinear nature of the heat sources. Thus, a specific model is developed for heat generation Q_{gen}, which computes reversible,
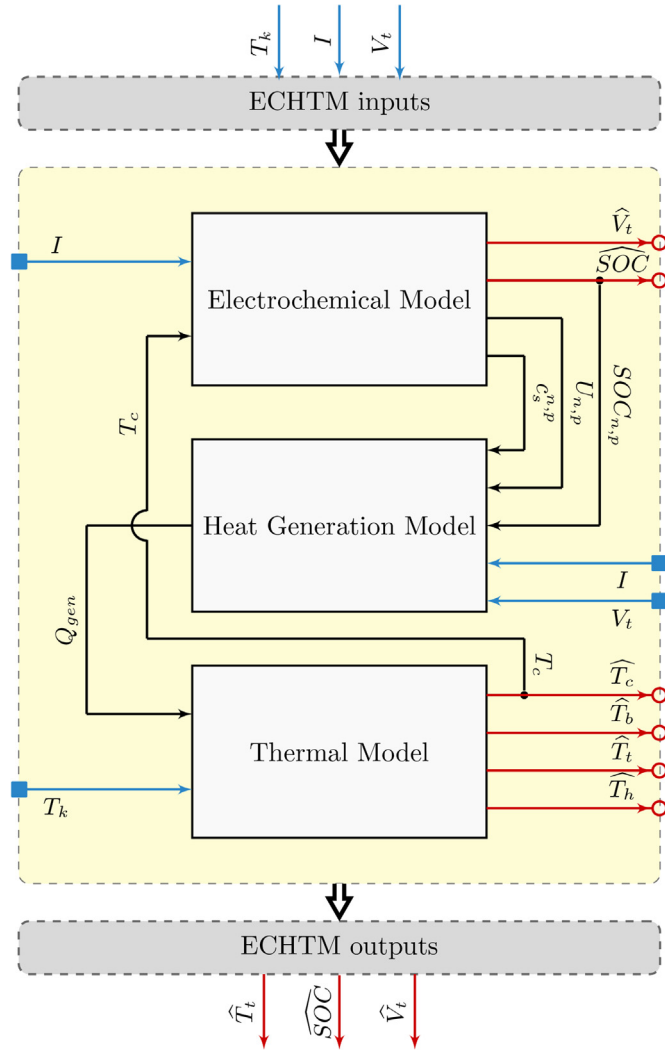
Fig. 1. Diagram of the combined electrochemical, heat generation and thermal model (ECHTM) modeling approach.

irreversible, and heat of mixing losses, as a function of the measured terminal voltage, the measured current, the modeled $SOC_{p,n}$, the modeled $U_{p,n}$, and the concentration gradients $C_s^{n,p}$ determined by the electrochemical model. Finally, the 4NTM model evaluates the temperatures of the core T_c, bottom T_b, terminal T_t, and housing T_h as a function of the heat generation rate, cooler temperature T_k, cell's geometry and boundary conditions. The experimental results shown in section 7 and 8, indicates a relatively small difference between the housing and the core temperature of 2 °C. Hence, only the core temperature information is then fed back to update the electrochemical model. This iterative procedure is repeated at every time step to model the cell in real time continuously.

In Fig. 1 the blue arrows represent inputs, the black arrows represent internal variables, and the red arrows represent outputs. The colored-doted blocks represent software functions. The combined ECHTM inputs are data provided by the vehicle sensors, and the outputs are processed data transferred to the main BMS.

In this section, the general formulation of the combined ECHTM is presented. In the following sections, the three sub-models are discussed in details.

3. Electrochemical battery model

3.1. Lithium-ion batteries principles of operation

Fig. 2 shows the basic setup of a battery cell. It consists of four main parts: the positive electrode (cathode), the separator, the electrolyte, and the negative electrode (anode). The battery is connected to an external load using current collector plates. The anode is usually made up of a mixture of carbon (e.g. Li_xC_6), the cathode is typically made of metal oxides (ex. $LiCoO_2$ or $LiMn_2O_4$), while the electrolyte can be made of a salt-containing solvent mixture, polymer, or solid materials (e.g. $LiPF_6$).

Under the presence of a load current, reduction-oxidation reaction occurs. Oxidation reaction takes place at the anode where the trapped lithium particles start to deintercalate or diffuse toward the electrolyte-solid interface splitting lithium into ions and electrons. Lithium ions transfer through the solution due to the potential difference while the electrons move through the current collector because the electrolyte solution serves as a barrier to electrons. Reduction reaction takes place at the cathode where the
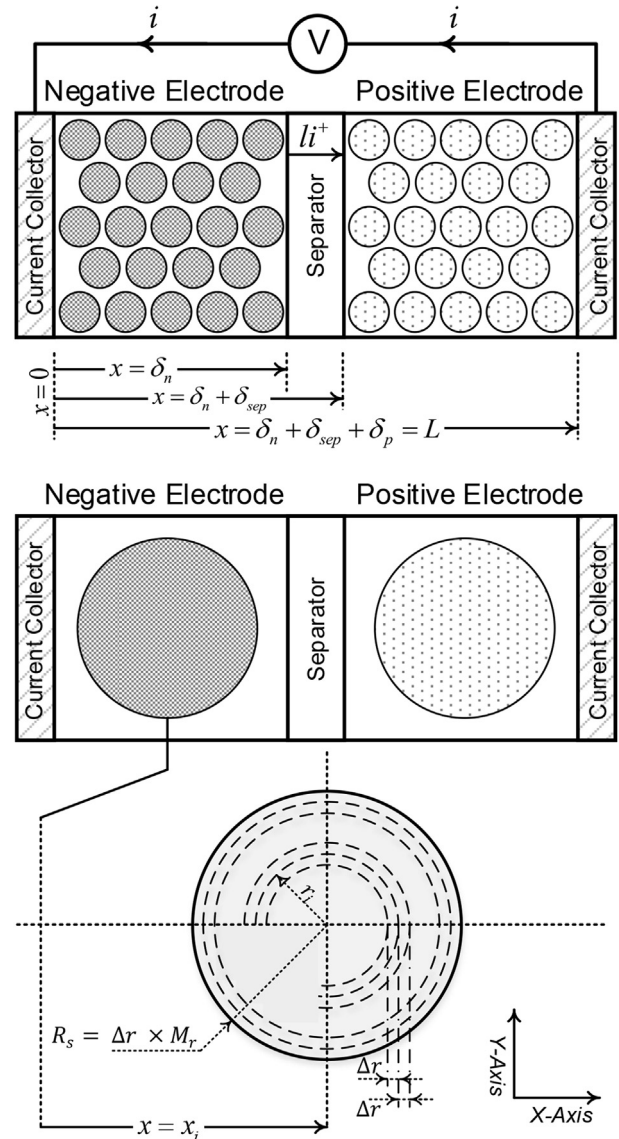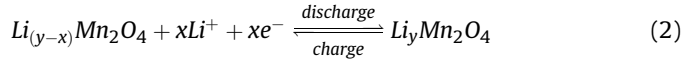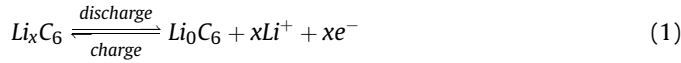

Fig. 2. Schematic representation of the Li-ion battery operation principles and the single particle model simplification.

traveling lithium ions from the anode start to intercalate and react with the electrons coming from the positive collector. An example of the electrochemical reactions are as follows:

$$Li_xC_6 \underset{charge}{\overset{discharge}{\rightleftharpoons}} Li_0C_6 + xLi^+ + xe^- \tag{1}$$

$$Li_{(y-x)}Mn_2O_4 + xLi^+ + xe^- \underset{charge}{\overset{discharge}{\rightleftharpoons}} Li_yMn_2O_4 \tag{2}$$

The process of lithium ion insertion into the electrode happens without a change in the electrode crystal structure "intercalation" mechanism. The whole phenomenon of intercalation and deintercalation is reversible as lithium ions pass back and forth between the electrodes during charging and discharging. In theory, this phenomenon could go on infinitely. Unfortunately, due to cell material degradation and other irreversible chemical reactions, the cell capacity and power degrade with the number of cycles and usage.

3.2. Model mathematical formulation

3.2.1. Relationship between concentrations and currents
The mathematical equations governing the charge and mass conservation in the solid and electrolyte phases is discussed in details in Ref. [32] and summarized in Table 1.

3.2.2. Butler-Volmer kinetics equations
The Butler-Volmer current density equation governs the volumetric rate of the chemical reaction. This equation links the four conservation equations ((3), (6), (9) and (12)) and is described as [32]:

$$j^{li} = a_s j_0 \left[\exp\left(\frac{\alpha_a F}{RT} \eta \right) - \exp\left(-\frac{\alpha_c F}{RT} \eta \right) \right] \tag{15}$$

where the overpotential η is defined as:

$$\eta = \phi_s - \phi_e - U(c_{se}) \tag{16}$$

and the coefficient j_0 is a function of the surface electrolyte concentration c_{se} and obtained as:

$$j_0 = (c_e)^{\alpha_a} \left(c_{s,max}^{n,p} - c_{se}^{n,p} \right)^{\alpha_a} \left(c_{se}^{n,p} \right)^{\alpha_c} \tag{17}$$

Finally, the cell potential, V, across the cell terminals is determined as follows:

$$V = \phi_s(x = L) - \phi_s(x = 0) - R_f \frac{I}{A} \tag{18}$$

3.3. Model reduction

Due to the computational complexity of the Full Order Model (FOM) some assumptions and simplifications are considered in order to obtain a Reduced Order Model (ROM).

The simplification assumptions are as follows: (i) the lithium concentration in electrolyte c_e is assumed to be constant and uniform. (ii) the solid particle distribution along the electrode is neglected, this is due to the averaging procedure in the first assumption. (iii) the aging dependencies of the model parameters have been neglected. As a result of the assumptions mentioned above, a single particle from each electrode (anode and cathode) can describe the diffusion dynamics.

$$\frac{\partial c_s^{n,p}(r,t)}{\partial t} = \frac{D_s}{r^2} \frac{\partial}{\partial r} \left[r^2 \frac{\partial c_s^{n,p}(r,t)}{\partial r} \right] \tag{19}$$

$$c_e(x,t) = \bar{c}_e \tag{20}$$

$$\sigma^{eff} \frac{\partial^2}{\partial x^2} \phi_s(x,t) = \bar{j}_{n,p}^{li} \tag{21}$$

Table 1
Set of PDEs equations describing the full-order electrochemical model and its boundary and initial conditions.

Conservation equations	Boundary conditions	Initial conditions
Mass transport in the solid phase		
$\frac{\partial c_s^{n,p}(x,r,t)}{\partial t} = \frac{D_s}{r^2} \frac{\partial}{\partial r} \left[r^2 \frac{\partial c_s^{n,p}(x,r,t)}{\partial r} \right]$ (3)	$\left. \frac{\partial c_s^{n,p}}{\partial r} \right|_{r=0} = 0,$ $\left. \frac{\partial c_s^{n,p}}{\partial r} \right|_{r=R_s^{n,p}} = \frac{-j^{li}}{D_s a_s F}$ (4)	$c_s^{n,p}(x,r,t_0) = c_{s_0}^{n,p}(x,r)$ (5)
Mass transport in the electrolyte		
$\frac{\partial \varepsilon_e c_e(x,t)}{\partial t} = D_e^{eff} \frac{\partial^2 c_e(x,t)}{\partial x^2} + \frac{1-t_0^+}{F} j^{li}$ (6)	$\left. \frac{\partial c_e^n}{\partial x} \right|_{x=0} = 0, \left. \frac{\partial c_e^p}{\partial x} \right|_{x=L} = 0$ (7)	$c_e(x,t_0) = c_{e_0}(x)$ (8)
Potential in the solid electrodes		
$\sigma^{eff} \frac{\partial^2}{\partial x^2} \phi_s(x,t) = j^{li}$ (9)	$\left. \frac{\partial}{\partial x} \phi_s(x,t) \right|_{x=0,L} = \frac{-I}{A\sigma^{eff}}$ $\left. \frac{\partial}{\partial x} \phi_s(x,t) \right|_{x=\delta_n, \delta_n + \delta_{sep}} = 0$ (10)	$\phi_s(x,t_0) = \phi_{s,0}(x)$ (11)
Potential in the electrolyte		
$\kappa^{eff} \frac{\partial^2}{\partial x^2} \phi_e(x,t) + \kappa_D^{eff} \frac{\partial^2}{\partial x^2} \ln c_e = -j^{li}$ (12)	$\left. \frac{\partial}{\partial x} \phi_e(x,t) \right|_{x=0,L} = 0$ (13)	$\phi_e(x,t_0) = \phi_{e,0}(x)$ (14)

$$\kappa^{eff}\frac{\partial^2}{\partial x^2}\phi_e(x,t) = -\bar{j}^{li}_{n,p} \tag{22}$$

$$\bar{j}^{li}_{n,p} = \frac{I}{A\delta_{n,p}} \tag{23}$$

The ROM is summarized in equation (19)–(23). The terminal voltage can be rewritten by substituting equation (16) in equation (18), as shown in Ref. [33]:

$$V(t) = [U_p(\theta_p) - U_n(\theta_n)] + \vartheta^{n,p}_\eta(\theta_{n,p}, I) - IK_{res} \tag{24}$$

where K_{res} is described as follows:

$$K_{res} = \frac{R_f}{A} - (\bar{\phi}^p_e - \bar{\phi}^n_e) = \frac{1}{A}\left[R_f + \frac{(\delta_n + 2\delta_{sep} + \delta_p)}{2\kappa^{eff}}\right] \tag{25a}$$

where $\quad \bar{\phi}^p_e - \bar{\phi}^n_e = -\frac{1}{2A\kappa^{eff}}(\delta_n + 2\delta_{sep} + \delta_p) \tag{25b}$

The term $\vartheta^{n,p}_\eta(\theta_{n,p}, I)$ in equation (24) is the difference between the cathode and anode overpotentials, and can be calculated by substituting equation (23) in (15), $a^{n,p}_s = 3\varepsilon^{n,p}_s / R^{n,p}_s$, and $\alpha_a = \alpha_c = 0.5$ from Table 3, as shown below:

$$\vartheta^{n,p}_\eta(\theta_{p,n}, I) = \bar{\eta}_p - \bar{\eta}_n = \frac{RT}{\alpha_a F}\ln\frac{\xi_p + \sqrt{\xi^2_p + 1}}{\xi_n + \sqrt{\xi^2_n + 1}} \tag{26a}$$

where $\quad \xi_{n,p} = \Omega^{n,p}\dfrac{I}{\left(c^{n,p}_{s,max}c^{n,p}_{se} - c^{n,p^2}_{se}\right)^{0.5}} \tag{26b}$

and $\quad \Omega^{n,p} = \dfrac{R^{n,p}_s}{6A\delta_{n,p}\varepsilon^{n,p}_s(\bar{c}_e)^{0.5}} \tag{26c}$

The term $U_p(\theta_p) - U_n(\theta_n)$ in equation (24) is the difference between the open circuit voltage for the anode and cathode. The stoichiometry ratio $\theta_{n,p}$ is the normalized solid-electrolyte interface concentration for the anode and cathode respectively.

$$\theta_{n,p} = \frac{\bar{c}^{n,p}_{s,e}}{c^{n,p}_{s,max}} \tag{27}$$

where $\bar{c}^{n,p}_s$ is the average bulk concentration and can be obtained as follows [32]:

Table 2
Properties of the lithium-ion cell under test.

Parameter	Value	Unit
Anode material	Graphite	–
Cathode material	NMC	–
Nominal voltage	4.25	V
Nominal capacity	26	Ah
Cell length	17.2	cm
Cell width	2.4	cm
Cell height	9.6	cm

Table 3
Model parameters - constant parameters and formula-based parameters.

Symbol	Value		
	Anode	Separator	Cathode
α_a, α_c	0.5	–	0.5
σ	1	–	0.1
σ^{eff}	$\sigma^{eff} = \varepsilon^{n,p}_s \sigma$	–	$\sigma^{eff} = \varepsilon^{n,p}_s \sigma$
$a^{n,p}_s$	$a^n_s = \frac{3\varepsilon^{n,p}_s}{R_s}$	–	$a^p_s = \frac{3\varepsilon^{n,p}_s}{R_s}$
κ	$\kappa = 0.0158c_e e^{(0.85c^{1.4}_e)}$		
κ^{eff}	$\kappa^{eff} = \varepsilon^{n,p}_s \kappa$		

$$\bar{c}^{n,p}_s(t) = \frac{3}{R^3_s}\int_0^{R_s} r^2 c^{n,p}_s(r,t)dr \tag{28}$$

The cell SOC and nominal capacity are defined as follows:

$$SOC = \frac{\theta_{n,p} - \theta_{0\%}}{\theta_{100\%} - \theta_{0\%}} \tag{29}$$

$$C_{nom} = \frac{AF\delta_{n,p}\varepsilon^{n,p}_s c^{n,p}_{s,max}[\theta^{n,p}_{100\%} - \theta^{n,p}_{0\%}]}{3600}, \quad [Ah] \tag{30}$$

3.4. State-space formulation

In order to the ROM to be useful for control and systems engineering, the PDEs must be rewritten in state-space representation. First, the model is discretized using the central finite difference method (CFDM), then a state-space representation is formulated.

By using the CFDM for the radial dimension r, it is possible to describe the spherical PDE by a set of ordinary differential equations (ODE). Equation (19) can be written as

$$\frac{\partial c_s(r,t)}{\partial t} = D_s\left(\frac{\partial^2 c_s}{\partial r^2} + \frac{2\partial c_s}{r\partial r}\right) \tag{31}$$

By discretizing the solid spherical particle into M_r shells along the radial dimension r as shown in Fig. 2, such that $R_s = \Delta r \times (M_r)$, and defining $q = 1, ..., M_{r-1}$ where $r_q = q \times \Delta r$ equation (31) becomes:

$$\dot{c}^{n,p}_s\Big|_q = \frac{D_s}{\Delta r^2}\left[\left(\frac{q-1}{q}\right)c^{n,p}_s\Big|_{q-1} - 2c^{n,p}_s\Big|_q + \left(\frac{q+1}{q}\right)c^{n,p}_s\Big|_{q+1}\right] \tag{32}$$

The boundary condition equation (4) can be rewritten accordingly:

$$c^{n,p}_s\Big|_0 = c^{n,p}_s\Big|_1 \tag{33}$$

$$c^{n,p}_s\Big|_{M_r} = c^{n,p}_s\Big|_{M_{r-1}} + \Delta r\frac{-\bar{j}^{li}}{Fa_s D_s} = c^{n,p}_{se} \tag{34}$$

By substituting with the boundary conditions equations (33) and (34), and rearranging, a state-space representation for equation (32) can be formulated as follows:

$$\dot{c}^{n,p}_s = \mathbf{A}c^{n,p}_s + \mathbf{B}j^{li} \tag{35}$$

$$c^{n,p}_{se} = c^{n,p}_s\Big|_{M_r} = c^{n,p}_s\Big|_{M_{r-1}} + \mathbf{D}j^{li} \tag{36}$$

where the state-space matrices, A, B, and D, are obtained as follows:

$$\mathbf{A} = \Psi \begin{bmatrix} -2 & \dfrac{q+1}{q} & 0 & \cdots & 0 & 0 \\ \dfrac{q-1}{q} & -2 & \ddots & & 0 & 0 \\ 0 & \ddots & \ddots & \ddots & & \vdots \\ \vdots & & \ddots & \ddots & \ddots & 0 \\ 0 & 0 & & \ddots & -2 & \dfrac{q+1}{q} \\ 0 & 0 & \cdots & 0 & \dfrac{q-1}{q} & -\dfrac{q-1}{q} \end{bmatrix} \qquad (37)$$

$$\mathbf{B} = Z \begin{bmatrix} 0 \\ 0 \\ 0 \\ \vdots \\ \vdots \\ \dfrac{q+1}{q} \end{bmatrix} \qquad (38)$$

$$\mathbf{D} = -\frac{Z}{\Psi} \qquad (39)$$

where $\Psi = D_s/\Delta r^2$ and $Z = 1/(\Delta r \times a_s \times F)$. The lithium concentration in the solid particle at the outer shell when $r = M_r$ is referred to as the lithium concentration at the solid-electrolyte interface $c_{se}^{n,p}$.

In this publication, the SPM is discretized into four shells $M_r = 4$. This reduces to model's state-space system to 3 states, and one output equation. The computational cost of the system in terms of CPU simulation time is approximately 1.2 s for every 25 min in real time. The CPU times presented in this publication were run on a 2.30 GHz Intel processor with 16 GB RAM.

3.5. Thermal dependent parameters

The cell temperature varies due to nonisothermal operating conditions. Arrhenius equation governs the most significant temperature-dependent parameters such as solid phase diffusion coefficient, electrolyte ionic conductivity, electrolyte diffusional ionic conductivity.

$$\psi = \psi_{ref} exp \left[\frac{E_{act}^{\psi}}{R} \left(\frac{1}{T_{ref}} - \frac{1}{T} \right) \right] \qquad (40)$$

where ψ is temperature dependent model parameter, ψ_{ref} is its value at T_{ref}, R is the universal gas constant and E_{act}^{ψ} is the activation energy. The fitted results for the solid diffusion coefficient and internal resistance were found to follow an Arrhenius relationship with temperature. The results are plotted in Fig. 3, where the gray points represent the data points, and the solid-blue line represents the data fit.

4. Heat generation model

Energy conversion losses through electrical, chemical and mass transport processes are responsible for the heat generation experienced during the cell's operation. In the literature, various ways have been utilized to model the heat generation rate ranging from analytical to experimental approaches. The analytical approach as discussed by Bernadi et al. [34] calculates the heat generation rate using an energy balance that accounts for different sources of heat generation. Whereas, experimental approaches measures the heat generation rate using calorimetry techniques as described by Kobayashi et al. [35].

In this publication, the analytical approach will be considered due to the nature of our application. A complete expression for the heat losses that accounts for all the chemical reactions, mixing processes, polarization effects and electrode kinetics is often impractical. A simplified formulation derived by Berandi et al. [34] is widely used in literature. Bernardi's expression quantified the losses in an electrochemical system taking into account the enthalpy of the reactions, the enthalpy of mixing, the phase-change and the heat capacity.

The total heat sources $\dot{Q}_{gen}$ consist of four different terms and defined as follows:

$$\dot{Q}_{gen} = \dot{Q}_{rev} + \dot{Q}_{irr} + \dot{Q}_{mix} + \dot{Q}_{sr} \qquad (41)$$

4.1. Reversible losses

The first term in equation (41) is the reversible losses ($\dot{Q}_{rev}$) and can be calculated as shown in (42)

$$\dot{Q}_{rev} = IT \frac{\partial (U_p - U_n)}{\partial T} \qquad (42)$$

The magnitude of $\dot{Q}_{rev}$ can be either positive or negative depending on the sign of the entropic coefficient. The entropic coefficient $\partial U_{p,n}/\partial T$ quantifies the magnitude of the OCP dependency on temperature and is directly correlated with the entropy change and hence the reversible losses. A common way of calculating the entropic coefficient is to discharge the cell to a predefined SOC and wait until the cell relaxes to record the equilibrium potential and then repeat at different temperature points and different SOC points. This can either be done by keeping the SOC constant and then varying the temperature or by varying the SOC while holding the temperature constant, though the latter method results in more uncertainty [36]. The accuracy of the results depends on the number of SOC points considered. It can take extended experimental procedures to get sufficient data. Some novel approaches such as electrothermal impedance spectroscopy [37] as well as methods based on calorimetry [38] are discussed in the literature.

In this publication, the OCP-curve was calculated as the average of continuously charging/discharging the cell at $C/52$. At such discharge rate, the cell is in quasi-equilibrium and the terminal voltage approximately equal to the real equilibrium value [39]. This method is convenient as it provides readings for the whole SOC range, but it can have a lower accuracy due to the relaxation effects. Tests were performed at [-25 °C, -10 °C, 0 °C, 10 °C, 25 °C, and 40 °C]. The entropic coefficient was then obtained by performing a linear fit to each SOC point against the six available temperatures. To obtain the entropic coefficient for both the cathode and anode separately, the value for the anode's entropic coefficient was obtained from Kumaresan et al.'s publication [40], while the cathode's entropic coefficient was calculated using equation (43).

$$\frac{\partial U}{\partial T_p} = \frac{\partial OCV}{\partial T} + \frac{\partial U}{\partial T_n} \qquad (43)$$

The experimental results obtained can be found in Fig. 4. The experimental procedure for obtaining the electrode's OCP curves will be discussed in Section 7.
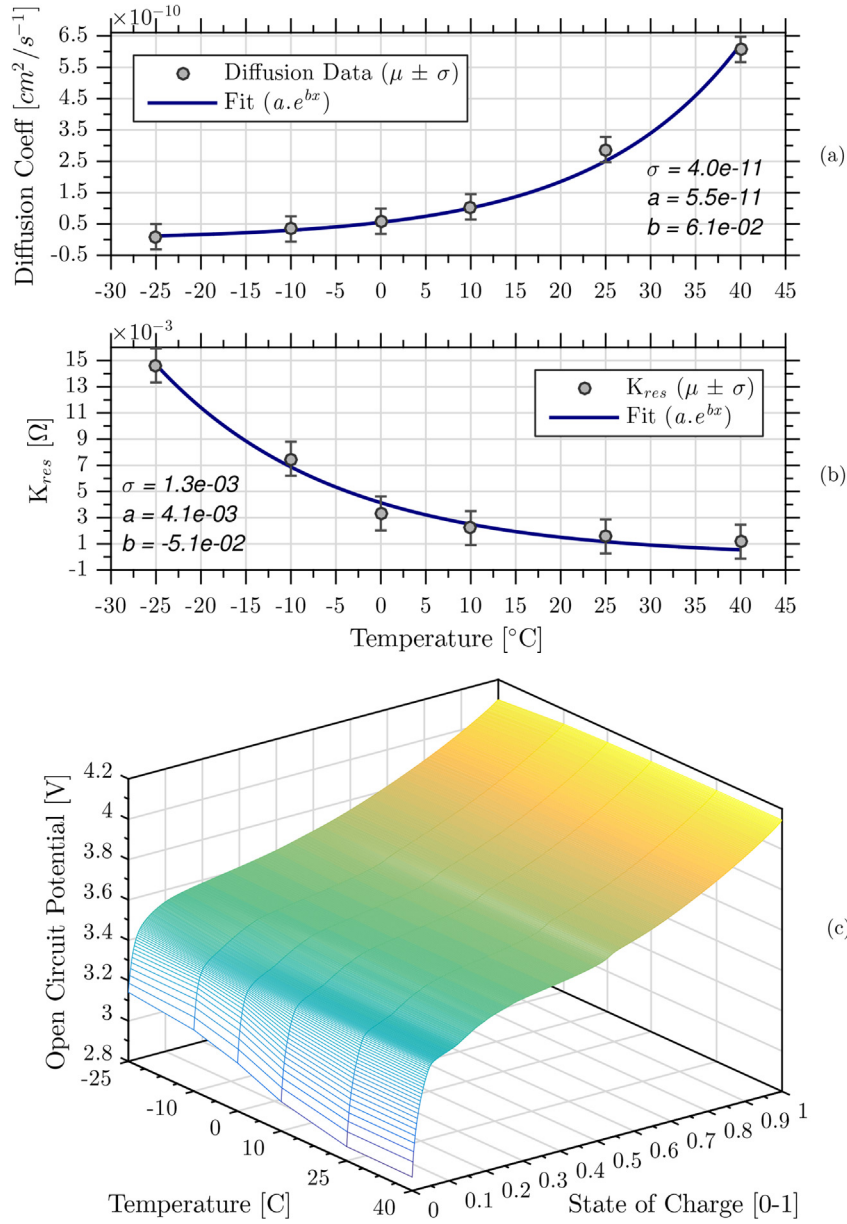
Fig. 3. Temperature dependent parameters (a) Solid-phase diffusion coefficient (b) Internal resistance (c) Open circuit potential versus SOC.

4.2. Irreversible losses

The second term in equation (41) is the irreversible losses ($\dot{Q}_{irr}$) or the polarization losses. Polarization is the deviation of the cell's voltage from its equilibrium voltage due to the ohmic, activation and concentration polarization [41]. The irreversible loss is quantified by how much the instantaneous cell potential deviates from the equilibrium potential and can be calculated as shown in (44). Losses induced by polarization have the biggest magnitude out of all the modes of losses.

$$\dot{Q}_{irr} = I[V_t - (U_p - U_n)] \tag{44}$$

4.3. Heat of mixing

The third term in equation (41) is the heat of mixing ($\dot{Q}_{mix}$), and it models the losses released or absorbed from the formation and

relaxation of the concentration gradients during the operation of a lithium-ion cell. The heat of mixing in porous insertion electrodes can be divided into four modes (i) the concentration gradients inside the spherical particles, (ii) concentration gradients inside the bulk electrolyte, (iii) concentration gradients inside the electrolyte pores of the insertion electrode, and (iv) concentration gradients inside the bulk electrode.

The heat of mixing within the spherical particles has the biggest magnitude out of these four modes and its formula as derived by Thomas et al. [42] is expressed in equation (45). This formula was derived using a Taylor-series expansion for the molar enthalpy of each species while neglecting the effects of pressure and density change and assuming the magnitude of the second derivative of the partial molar enthalpy to be negligible.

$$\Delta H = \frac{1}{2c_{b,\infty}\overline{V}_{b,\infty}} \frac{\partial H_A}{\partial c_a} \int (c_a - c_{a,\infty})^2 dv \tag{45}$$
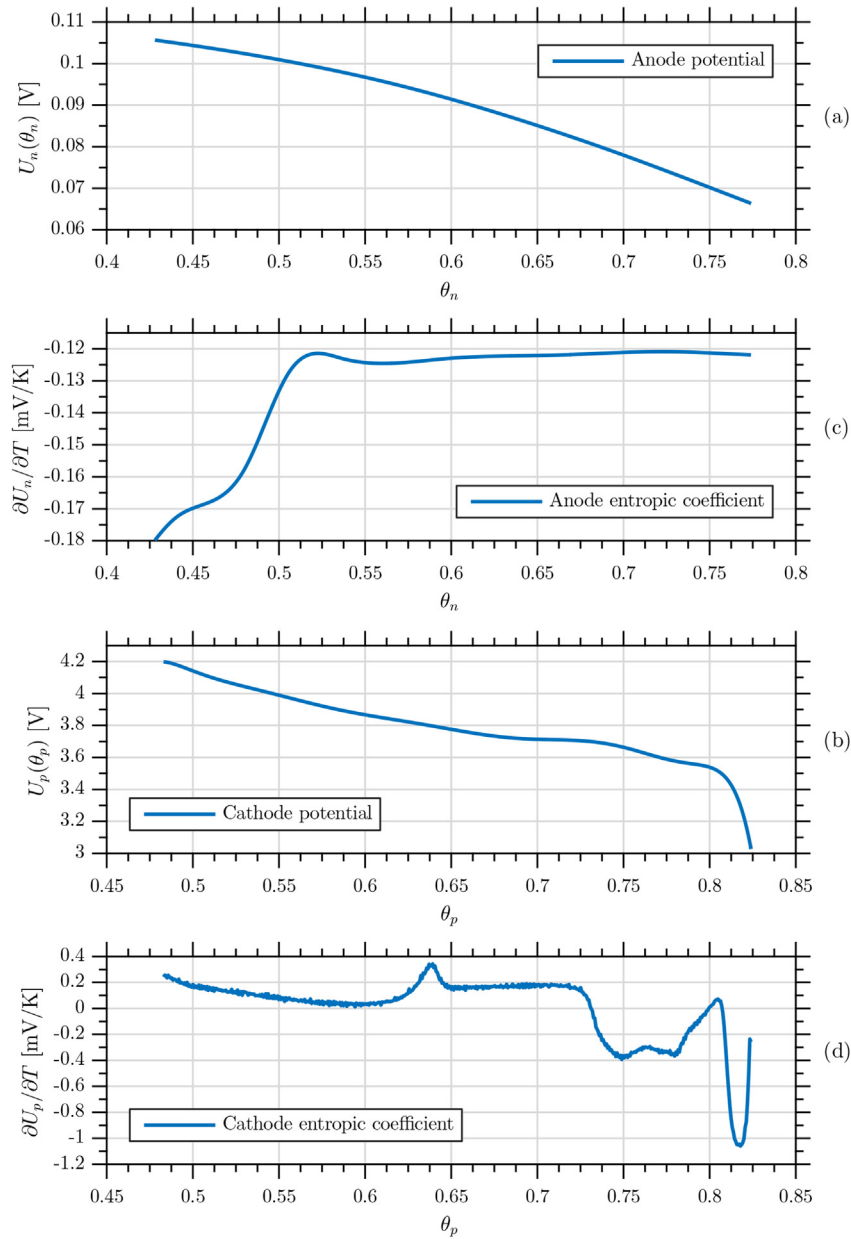
Fig. 4. OCP for the (a) Anode, (b) Cathode and the entropic coefficient for the (c) Anode, (d) Cathode.

where $c_{b,\infty}$ & $\overline{V}_{b,\infty}$ are the volume-averaged concentration and partial molar volume of species 'b', the product $c_{b,\infty}\overline{V}_{b,\infty}$ was assumed to be 1 [43]. $\partial H_a/\partial c_a$ is the change in enthalpy of mixing for species 'a' per change of concentration and can be calculated as follows:

$$\frac{\partial H_A}{\partial c_a} = -F\frac{\partial U_H}{\partial c_a} \tag{46}$$

where

$$U_H = U - T\frac{dU}{dT} \tag{47}$$

The coefficient $\partial H_A/\partial c_a$ is calculated using numerical differentiation of (47), where U_H is calculated using the knowledge of the OCP and the entropic coefficient of the negative and positive

electrodes. The integral in (45) is approximated using the trapezoidal rule:

$$\int (c_A - c_{A,\infty})^2 dv = \int (c_A - c_{A,\infty})^2 4\pi r^2 dr$$
$$= \sum_{i=1}^{n-1} 2\pi\Delta r\left[r_i^2\left(c_i - c_{avg}\right)^2 + r_{i+1}^2\left(c_{i+1} - c_{avg}\right)^2\right] \tag{48}$$

The power released due to this change of enthalpy during time step Δt is expressed as:

$$\dot{Q}_{mix} = \frac{\Delta H}{\Delta t} \tag{49}$$

Using (49) and (45) the heat of mixing can be calculated

follows:

$$\dot{Q}_{mix} = \frac{\partial}{\partial t}\left[\frac{1}{2}\frac{\partial H_A}{\partial c_a}\int (c_a - c_{a,\infty})^2 dv\right] \qquad (50)$$

4.4. Side reactions

The fourth term in equation (41) is the heat associated with any side reactions that may occur ($\dot{Q}_{sr}$). During normal operating conditions, this term can be neglected as discussed in Ref. [34].

Fig. 7-c and 7-j shows the magnitude of each heat losses component based on the parameterization cycle and the validation cycle, respectively. The parameterization and validation are discussed later in Section 7. The irreversible losses have the biggest magnitude out of all the total heat losses. While the reversible losses is the second biggest of heat losses. Finally, the heat of mixing losses is negligible compared to the reversible and irreversible losses. This agrees with Thomas et al. [42] findings of the negligibility of the heat of mixing for porous insertion electrodes in well-designed cells. Now that an estimate of the heat flux can be calculated, a temperature model, therefore, has to be defined to translate the losses and the boundary conditions into the cell's temperature.

5. Thermal model

5.1. Model mathematical formulation

This section introduces the thermal model of the combined ECHTM. Due to the nature of the application and to reduce the model computational complexity, the detailed geometry of the cell's internal components were not considered and were simply abstracted by a simple 0-D model with four nodes. The four nodes lumped capacitance model is developed to capture the thermal behavior of the prismatic cell adequately as shown in Fig. 5-a. The terminal node represents the average temperature of the positive and negative terminals. The bottom node represents the temperature change in the cell due to the temperature gradient caused by the cooling. The housing node captures the heat conduction of the outer housing shell. Finally, the core node represents the change in the core temperature of the cell.

Due to the cell's geometry, experimental setup, thermal properties, and temperature range of operation, the following assumptions and simplifications have been proposed. (i) Thermal properties are assumed to be independent of temperature since the operational temperature range of the cell is too small to show any significant dependence of the material thermal properties on temperature. (ii) The cell's core, housing, bottom, and terminals are each represented by a heat capacitor. (iii) The heat transfer from convection and radiation were assumed to be negligible.

The heat generation due to the electrochemical reaction is assumed to be localized in the cell's core, whereas the resistive losses due to the tab and current collector losses are assumed to be confined in the cell's terminal. Based on these assumptions, the heat flux due to the cell's operational losses is generated at both the terminal and the core. For each of the four nodes an ordinary differential equation (energy balance) expresses the heat exchange paths and the boundary conditions.

At the terminals, there is heat transfer to and from the core and the housing along with the losses P_t^{th} originating from the tap's restrictive losses.

(a)
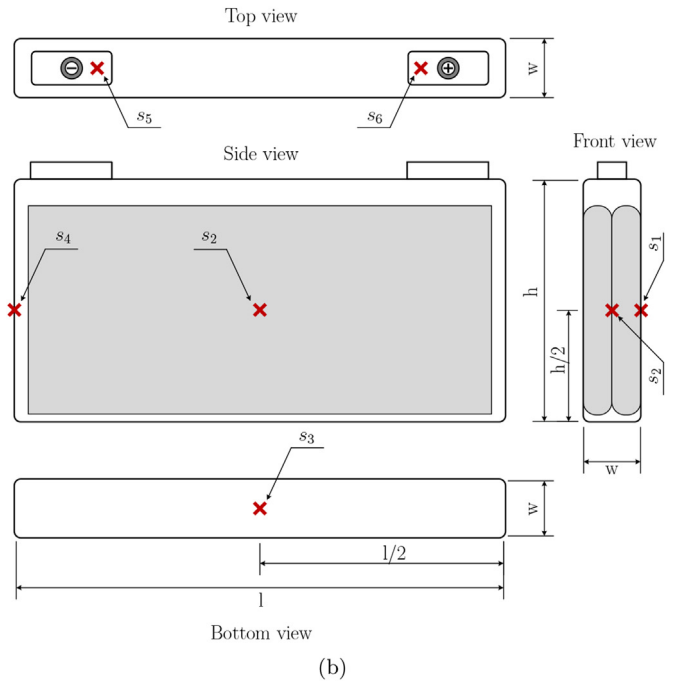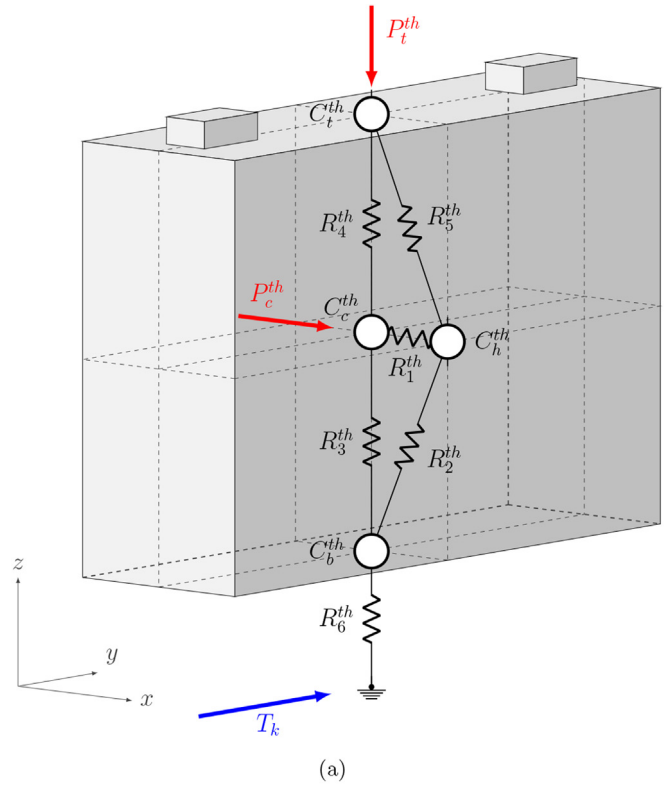
Fig. 5. (a) A visual representation of the lumped temperature model of a prismatic cell, (b) Internal and external sensor locations.

$$C_t^{th}.\dot{T}_t = \frac{T_c - T_t}{R_4^{th}} + \frac{T_h - T_t}{R_5^{th}} + P_t^{th} \qquad (51)$$

where P_t^{th} is determined experimentally through considering the resistivity values for both the cathode (Aluminum) and anode (copper) terminals along with the physical dimensions of the current collectors.
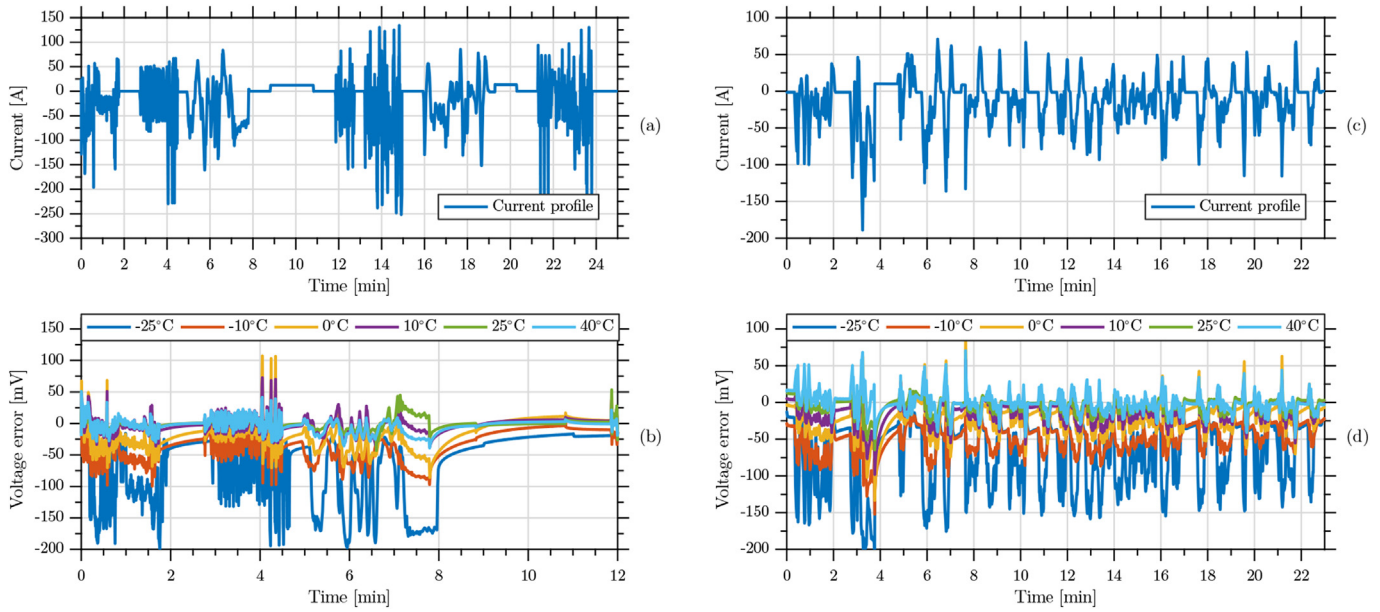
Fig. 6. Electrochemical model (a) Parameterization cycle - current profile at 25 °C (b) Parameterization cycle - voltage error at different temperatures (c) Validation cycle - current profile at 25 °C (d) Validation cycle - voltage error at different temperatures.

Similarly, at the housing heat is exchanged with the terminal, core and bottom nodes as the housing is in contact with all the nodes.

$$C_h^{th} . \dot{T}_h = \frac{T_b - T_h}{R_2^{th}} + \frac{T_c - T_h}{R_1^{th}} + \frac{T_t - T_h}{R_5^{th}} \tag{52}$$

At the core (sometimes referred to as the jellyroll), heat is exchanged with all the surrounding nodes and a significant heat flux is generated due to the losses at the core as described in section 4.

$$C_c^{th} . \dot{T}_c = \frac{T_b - T_c}{R_3^{th}} + \frac{T_t - T_c}{R_4^{th}} + \frac{T_h - T_c}{R_1^{th}} + P_c^{th} \tag{53}$$

The bottom node is in direct contact with the cooler underneath. Heat is exchanged through conduction to the cooler. A constant temperature boundary condition is assumed for the cooler, whose temperature is regulated by the cooling system's controller.

$$C_b^{th} . \dot{T}_b = \frac{T_k - T_b}{R_6^{th}} + \frac{T_c - T_b}{R_3^{th}} + \frac{T_h - T_b}{R_2^{th}} \tag{54}$$

Since both the thermal conductance and the heat capacity can be assumed to be physical constants, the system can be modeled using linear ordinary differential equations and represented in a state-space representation.

$$\dot{T} = \mathbf{A}^{th} T + \mathbf{B}^{th} u \tag{55}$$

$$T_t = \mathbf{C}^{th} T + \mathbf{D}^{th} u \tag{56}$$

where

$$\dot{T} = \begin{bmatrix} \dot{T}_t \\ \dot{T}_h \\ \dot{T}_c \\ \dot{T}_b \end{bmatrix} \tag{57}$$

$$u = \begin{bmatrix} P_c^{th} \\ P_t^{th} \\ T_k \end{bmatrix} \tag{58}$$

The state-space matrices, A, B, C and D, are obtained as follows:

$$A^{th} = \begin{bmatrix} -\dfrac{1}{C_t^{th}}\left(\dfrac{1}{R_4^{th}} + \dfrac{1}{R_5^{th}}\right) & \dfrac{1}{C_t^{th} R_5^{th}} & \dfrac{1}{C_t^{th} R_4^{th}} & 0 \\[2ex] \dfrac{1}{C_h^{th} R_5^{th}} & -\dfrac{1}{C_h^{th}}\left(\dfrac{1}{R_1^{th}} + \dfrac{1}{R_2^{th}} + \dfrac{1}{R_5^{th}}\right) & \dfrac{1}{C_h^{th} R_1^{th}} & \dfrac{1}{C_h^{th} R_2^{th}} \\[2ex] \dfrac{1}{C_c^{th} R_4^{th}} & \dfrac{1}{C_c^{th} R_1^{th}} & -\dfrac{1}{C_c^{th}}\left(\dfrac{1}{R_1^{th}} + \dfrac{1}{R_3^{th}} + \dfrac{1}{R_4^{th}}\right) & \dfrac{1}{C_c^{th} R_3^{th}} \\[2ex] 0 & \dfrac{1}{C_b^{th} R_2^{th}} & \dfrac{1}{C_b^{th} R_3^{th}} & -\dfrac{1}{C_b^{th}}\left(\dfrac{1}{R_2^{th}} + \dfrac{1}{R_3^{th}} + \dfrac{1}{R_6^{th}}\right) \end{bmatrix} \tag{59}$$
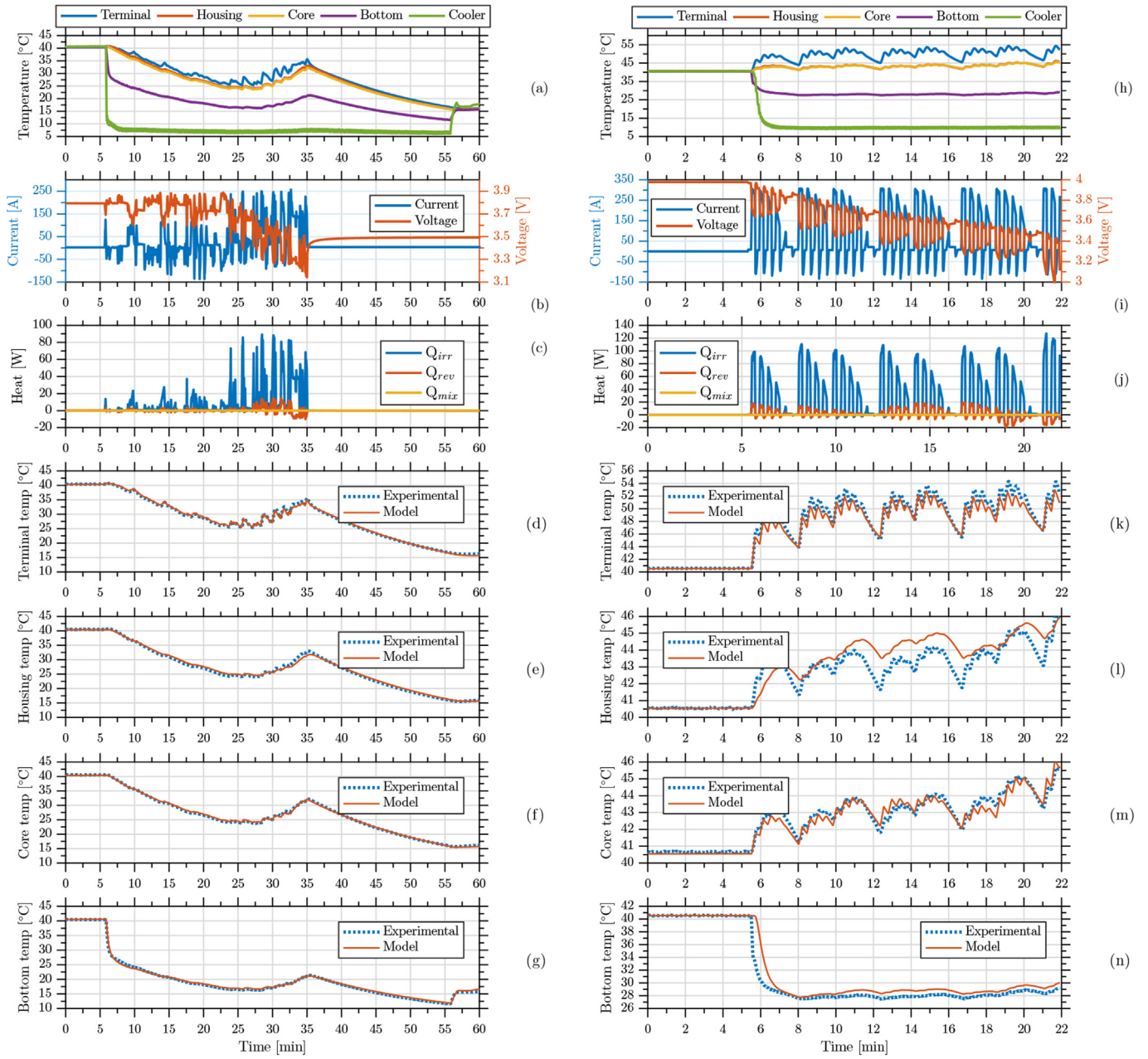
Fig. 7. On the left side the parameterization cycle (a) Temperature profiles (b) Current and voltage profile (c) Heat losses (d) Terminal temperature (e) Housing temperature (f) Core temperature (g) Bottom temperature, on the right side the validation cycle (h) Temperature profiles (i) Current and voltage profile (j) Heat losses (k) Terminal temperature (l) Housing temperature (m) Core temperature (n) Bottom temperature.

$$
\mathbf{B}^{\text{th}} = \begin{bmatrix} 0 & \dfrac{1}{C_t^{th}} & 0 \\[2mm] 0 & 0 & 0 \\[2mm] \dfrac{1}{C_c^{th}} & 0 & 0 \\[2mm] 0 & 0 & \dfrac{1}{C_b^{th} R_6^{th}} \end{bmatrix} \tag{60}
$$

$$
\mathbf{C}^{\text{th}} = \begin{bmatrix} 0 & 0 & 1 & 0 \end{bmatrix} \tag{61}
$$

$$
\mathbf{D}^{\text{th}} = [0] \tag{62}
$$

Equations (59)–(62) describe a linear time-invariant state-space system. The system's controllability and observability is described in equation (63) and equation (64) respectively.

$$
\mathbf{Co} = \begin{bmatrix} \mathbf{B} & \mathbf{AB} & \mathbf{A}^2\mathbf{B} & \mathbf{A}^3\mathbf{B} \end{bmatrix} \tag{63}
$$

$$
\mathbf{Ob} = \begin{bmatrix} \mathbf{C} & \mathbf{CA} & \mathbf{CA}^2 & \mathbf{CA}^3 \end{bmatrix}^T \tag{64}
$$

The system's controllability and observability matrices are full ranks.

6. Experimental setup

In this paper, two experimental setups were implemented. The experiments were conducted on a high-power prismatic lithium-ion battery cell to parameterize and validate each sub-model of the combined ECHTM. The prismatic cell under consideration contains a jelly roll core that consists of alternating layers of anode, separator, and cathode materials. The cell has an NMC-based cathode and graphite-based anode. The properties of the cell are given in Table 2.

In the first experimental setup, the experiment was performed using a Scienlab battery cycler with voltage accuracy of $\pm 0.05\%$ of the measured value, current accuracy of $\pm 0.05\%$ of the measured value, and temperature accuracy of $\pm 1\ K$. The voltage and current sensors are integrated to the cycler.

The thermocouples were installed both externally and internally in order to measure and validate the cell's temperature. The techniques of placing and protecting the internal thermocouple in order to ensure safety and accuracy of the measurements are discussed in details by Li et al. in Ref. [44]. The exact locations of the six internal and external thermocouples are illustrated in Fig. 5-b. The external thermocouples were attached using heat-resistant tapes at the locations shown. Whereas, the internal thermocouples locations were chosen to ensure the safety of the cells and the accuracy of the measurement. The internal thermocouples are required in order to validate the parameterized thermal model. The Scienlab cycler used during the experiment has 12 channels, four different current profiles were tested on 12 cells (one cell per channel). The tests were performed on a cluster of three cells under the same conditions, in order to minimize the impact of any cell manufacturing variations. The output of each cluster was averaged to obtain the required variables. In order to realize an isothermal condition for the experiment. The batteries were cycled inside a thermal chamber with a continuously controlled ambient temperature. The cell was directly exposed to the chamber air. Also, the thermocouples output was monitored continuously in real time and in case the temperature is 3 °C higher than the prescribed chamber temperature a wait buffer was introduced to the current profile.

In the second experimental setup, the tests were performed to parameterize the thermal model under non-isothermal conditions. During the test, in order to replicate the operating conditions in a battery pack of an electric/hybrid vehicle, the cells were placed in a closed container that minimized convection heat transfer. The container had an active cooler that ran below the cell that was directly in contact with the cell's bottom. Such tests allow the thermal dynamics of the prismatic cell to be captured. In order to mimic the vehicle operating conditions, the experiment had two controlled inputs, the cooler's temperature, and the current profile used to excite the cells.

In both setups, the measured variables are sampled every $100ms$ and then used as an input to the presented algorithm in the MATLAB/Simulink environment. Also, two cycles of C/52 CC-CV charge/discharge were conducted first in order to identify the cell's OCV and the nominal capacity of each cell.

The T_c is measured using the internal sensor (s_2), located at the core of the cell. Whereas, The T_b is measured by the external sensor (s_3), located at the bottom of the cell. Similarly, The T_h is calculated as the average of the two external temperature sensors (s_1 and s_4), located at the two sides of the cell. Finally, T_t is calculated as the mean of the two external temperature sensors (s_5 and s_6), located at the cell's negative and the positive terminals, respectively.

7. Parameter identification procedure

This section presents the procedure for identifying the electrochemical model and the thermal model parameters. The number of combined ECHTM parameters is relatively high if all of the parameters are considered as unknowns. In order to decrease the number of parameters to be identified, the parameterization process is divided into two steps.

In step one, the battery cell is operated under isothermal conditions using experimental inputs so as to limit the variations in the cell core temperature. The electrochemical dependent parameters are then identified at six different temperatures. The genetic algorithm (GA) was used to optimize the model parameters. The GA is theoretically proven to attain global convergence. The cost function of GA is to minimize the root mean squared error (RMSE) between the model terminal voltage output and experimental data at predefined temperature points.

In step two, the battery cell is excited under non-isothermal conditions using signals that are rich in the temperature range necessary to determine the thermal model parameters. The cost function of GA is to minimize the error between the model terminal, housing, bottom, and core temperature outputs and corresponding experimental data.

Table 3 summarizes the electrochemical model constants or formula-based parameters [33].

7.1. Identification of the electrochemical model parameters

In this step, a constant low-rate discharge/charge, and a highly dynamic driving cycle were used to identify the electrochemical model parameters. First, the low (C/52) discharge/charge was used to cycle the cell and the 3rd cycles was used to construct the V_{OCV} curve, to allow for SEI formation (Coulombic efficiency was in excess of 99% by this cycle). This step is used to identify the maximum electrode active material solid concentration and stoichiometry cycling range.

The negative electrode active material consists of graphite Li_xC_6. The correlation between the Li_xC_6 open-circuit potential and the negative electrode active material solid concentration has been measured in the laboratory as discussed by Farag et al. [32]. The $U_n(\theta_n)$ correlation is plotted in Fig. 4-a. The correlation between the open-circuit potential and the positive electrode active material solid concentration is plotted in Fig. 4-c and calculated by adding the $U_n(\theta_n)$ and the cell's measured open-circuit voltage as shown below:

$$U_p(\theta_p) = V_{OCV} + U_n(\theta_n) \tag{65}$$

Next, the highly dynamic driving cycle was used to identify the diffusion-related electrochemical model parameters. As shown in Fig. 6-a, the cycle contains charge-sustaining and charge-depleting phases, which makes it rich in the frequency content necessary to identify the cell parameters. The test starts with a fully charged battery and then a current profile is applied to discharge the battery until it is fully discharged.

The identified electrochemical model parameters, with their lower and upper bounds, are summarized in Table 4.

After the parametrization procedure by the GA, the model shows an accurate voltage prediction as shown in Fig. 6-b. The RMSE and MAE in the terminal voltage at the six different temperatures are summarized in Table 5.

7.2. Identification of the thermal model parameters

In this step, the battery is excited under non-isothermal conditions using the cycle shown in Fig. 7-a and 7-b. The thermal parameterization cycle is chosen to mimic real operating conditions. The cycle consists of three stages. First, the cooler is set to 5 °C

Table 4
Identified model parameters.

Symbol	Unit	Identified values	
		Anode	Cathode
$c_{s,max}^{n,p}$	mol cm^{-3}	0.072	0.080
$\theta_{0\%}$	–	0.428	0.824
$\theta_{100\%}$	–	0.774	0.483
$\varepsilon_s^{n,p}$	–	0.958	0.950
$R_s^{n,p}$	cm	0.00026	0.000475
A	cm^2	8833.9	
$\bar{c}_e$	mol cm^{-3}	3.13*1e2	
K_{res}	Ωcm^2	Fig. 3-a	
D_e^p	$cm^2 s^{-1}$	Fig. 3-b	

Table 5
Electrochemical model results at different temperature - RMSE and MAE [V].

Core temperature [±1.5 °C]	Parameterization cycle	
	RSME [V]	MAE [V]
−25 °C	0.072	0.066
−10 °C	0.056	0.051
0 °C	0.044	0.041
10 °C	0.037	0.034
25 °C	0.027	0.022
40 °C	0.012	0.009

and the cell is subjected to low current (0—2 C-rate). During this phase, the battery is cooling down since the net losses are less than the cooling effect. Next, the cell is subjected to high current (2—12 C-rate) while keeping the cooler at 5 °C. During this phase, the battery heats up. Finally, no current withdrawn from the battery and the battery is allowed to relax to a thermal equilibrium; the temperature of the different nodes eventually cool to the same temperature once the cooler is removed. This cycle sweeps through 25 °C temperature range of operation. The identified thermal parameters, with their lower and upper bounds, are summarized in Table 6.

After the identification procedure by the GA, the model shows an accurate temperature prediction as illustrated in Fig. 7-d, 7-e, 7-f, and 7-g. The RMSE and MAE in the terminal, housing, core, and bottom temperatures are summarized in Table 7.

8. Model validation under different driving profiles

In this section, the combined ECHTM model performance is compared with experimental data to demonstrate the effectiveness of the preceding methodology. The validation cycles in this section

Table 6
Thermal model parameters.

Symbol	Unit	Value		
		Identified	LB	UB
C_t^{th}	JK^{-1}	8.36	1	2000
C_h^{th}	JK^{-1}	36.5	1	2000
C_c^{th}	JK^{-1}	683	1	2000
C_b^{th}	JK^{-1}	47.0	1	2000
R_1^{th}	KW^{-1}	1.23	$1e-3$	500
R_2^{th}	KW^{-1}	63.0	$1e-3$	500
R_3^{th}	KW^{-1}	0.713	$1e-3$	500
R_4^{th}	KW^{-1}	193	$1e-3$	500
R_5^{th}	KW^{-1}	4.79	$1e-3$	500
R_6^{th}	KW^{-1}	0.918	$1e-3$	500

Table 7
Thermal model parameterization cycle results.

Symbol	Parameterization cycle	
	RSME [°C]	MAE[°C]
T_t	0.327	0.259
T_h	0.492	0.389
T_c	0.257	0.207
T_b	0.363	0.290

Table 8
Electrochemical model validation results at different temperature - RMSE and MAE [V].

Core temperature [±1.5 °C]	Validation cycle	
	RSME [V]	MAE [V]
−25 °C	0.074	0.055
−10 °C	0.032	0.025
0 °C	0.025	0.02
10 °C	0.022	0.017
25 °C	0.017	0.013
40 °C	0.015	0.014

are different from those utilized for the purpose of identification. The validation procedure is divided into three steps. First, the electrochemical model is validated under isothermal operating conditions at six different temperature points. Next, using the input of the validated electrochemical model along with the temperature dependent parameters, the thermal model is validated under non-isothermal operating conditions against the experimental thermal measurements. Finally, the combined ECHTM model is validated under non-isothermal operating conditions against the experimental voltage and temperature measurements.

8.1. Isothermal electrochemical model validation

The first step validates the electrochemical model under isothermal operating conditions at six different temperature points. Fig. 6-c shows the Urban Dynamometer Driving Schedule (UDDS) cycle used for validation. The cycle was repeated at six different temperatures points [-25 °C, −10 °C, 0 °C, 10 °C, 25 °C, 40 °C]. Under the UDDS cycle, the error between the calculated voltages of the ROM and the measured voltage is shown in Fig. 6-d. The RMSE at six different temperatures between the modeled voltage and the measured voltage over five consecutive cycles with 10 min' rest between cycles is summarized in Table 8.

8.2. Thermal model validation

The second set of validation data is a consecutive high charge and discharge pulses with constant cooling. The cycle sweeps the cell through 50% SOC and 20 °C temperature range of operation. The experimental temperature measurements for the five sensors,

Table 9
Thermal model validation cycle results.

Symbol	Validation cycle	
	RSME [°C]	MAE [°C]
T_t	0.901	0.675
T_h	0.810	0.591
T_c	0.305	0.245
T_b	1.286	0.718

the input current, and the output voltage are illustrated in Fig. 7-h and 7-i. The calculated thermal model outputs are compared to the experimentally measured temperature sensors. The experimental versus modeled terminal, housing, core, and bottom temperatures are compared in Fig. 7-k, 7-l, 7-m, 7-n, respectively. The blue-dotted line represents the experimental temperature, while the solid-orange represents the thermal model response. The RMSE and MAE are summarized in Table 9.
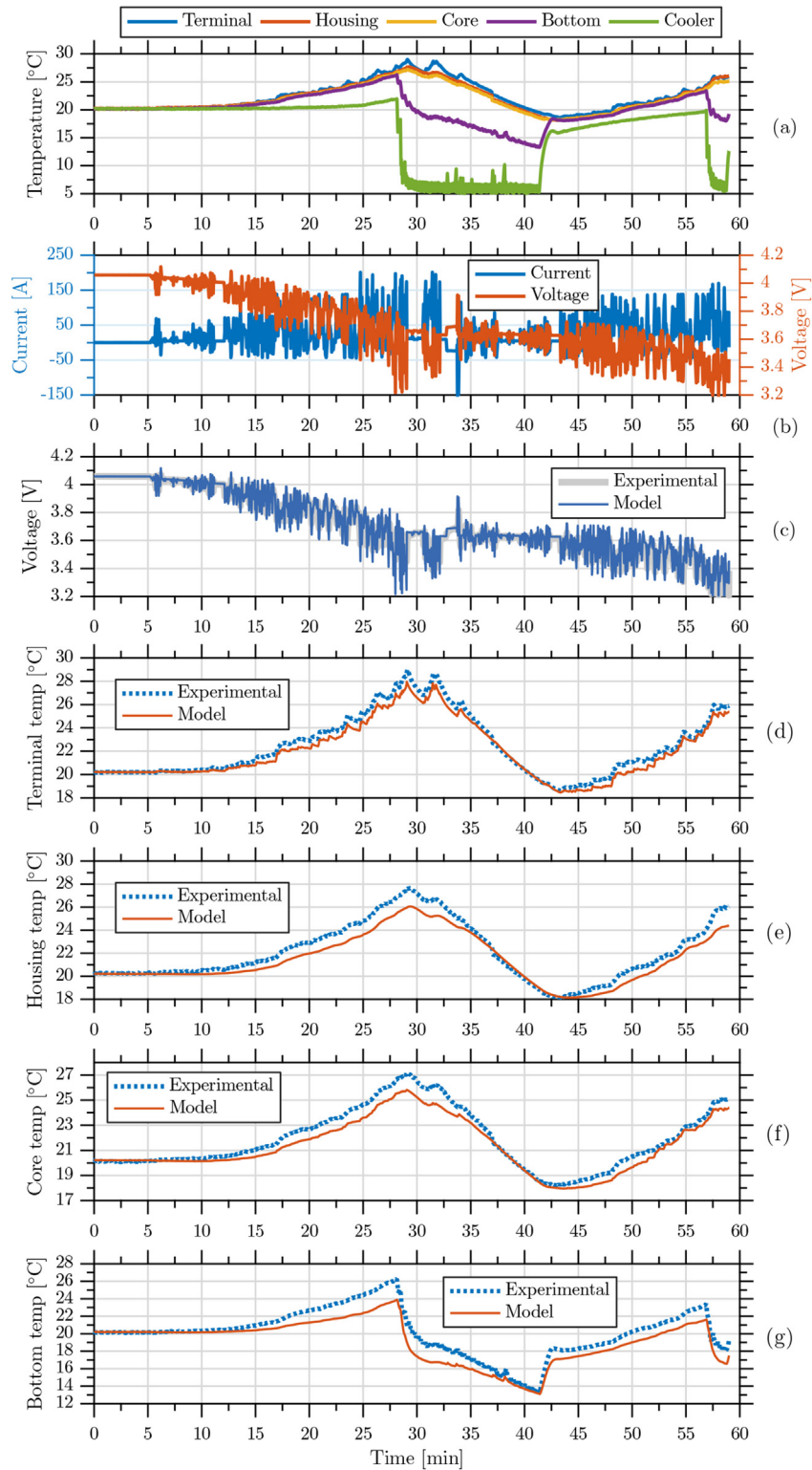

Fig. 8. Thermal model validation cycle (a) Temperature profiles (b) Current and voltage profile (c) Terminal voltage model versus measurements (d) Terminal temperature (e) Housing temperature (f) Core temperature (g) Bottom temperature.

8.3. Combined thermal-electrochemical model validation

The aim of the third set of validation is to validate the combined model. The cycle is rich in its temperature variation content and current frequency content. The cooler is turned on and off during operation as shown in Fig. 8-a. The current profile has a charge-sustaining, charge-depleting, and charging phases and sweeps the full SOC range and 20°C range of operation as illustrated in Fig. 8-b. Fig. 8-c shows the experimental voltage vs. the combined model output. The experimental versus modeled terminal, housing, core, and bottom temperatures are compared in Fig. 8-d, 8-e, 8-f, 8-g, respectively. The blue-dotted line represents the experimental temperature, while the solid-orange represents the thermal model response. The RMSE and MAE are summarized in Table 10.

9. Conclusion

In conclusion, a combined electrochemical, heat generation, and thermal model (ECHTM) is presented, which maintains terminal voltage and core temperature accuracy over a broad range of temperatures and state of charges. The temperature dependent electrochemical model considers the variations in the model parameters through Arrhenius equation. The proposed thermal model consists of lumped four thermal nodes interconnected by thermal resistances and capacitances. The heat generation model considers three sources of heat during operation (irreversible losses, reversible losses, and heat of mixing). The three models (electrochemical, heat generation, and thermal model) are coupled together in an iterative fashion to predict the cell's terminal voltage and core temperature accurately.

The electrochemical model parameters and the thermal model parameters are identified using a new technique that excites the model under isothermal and non-isothermal operating conditions, respectively. First, the electrochemical model with thermal dependent parameters was parameterized and validated under isothermal conditions at six different temperatures points [-25 °C, −10 °C, 0 °C, 10 °C, 25 °C, 45 °C]. It maintains a terminal voltage accuracy of ±80 mV at each temperature point. Next, the thermal model was parameterized and validated under non-isothermal conditions over a broad range of temperatures [-25 °C–45 °C]. It predicts the core temperature with an accuracy of ±2 °C. Finally, the combined ECHTM is validated under non-isothermal operating conditions, at different current rates, and temperature ranges.

The proposed combined ECHTM structure shows accurate terminal voltage and core temperature prediction at various operating conditions while maintaining a simple mathematical structure, making it ideal for real-time BMS applications. Future work will focus on using the electrochemical impedance spectroscopy (EIS) to investigate the dynamic behavior of the battery along with parameters sensitivity analysis. The use of calorimetry to quantify the heat generated within the cell. Also, incorporating iterative state of charge and core temperature estimation techniques (e.g. Extended Kalman Filter), along with developing a physics based aging model that accounts for power and capacity fade.

Nomenclature

Acronyms

$\overline{V}$	Partial molar volume(m^3mol^{-1})
A	State matrix in linear state-space model state equation
B	Input matrix in linear state-space model state equation
Co	Controllability matrix of a state-space model
D	Input matrix in linear state-space model output equation
Ob	Observability matrix of a state-space model
A	Electrode plate Area (cm^2)
a_s	Active surface area per electrode unit volume (cm^2cm^{-3})
c	Concentration of lithium ions ($molcm^{-3}$)
C^{th}	Average Heat capacity (JK^{-1})
D	Diffusion coefficient of lithium species (cm^2s^{-1})
E_{act}	Activation energy (J)
F	Farady's Constant (F = 96,487) (C mol^{-1})
H	Enthalpy (J)
h	Convection heat transfer coefficient($Wm^{-2}K^{-1}$)
I	Applied current (A)
j^{li}	Butler-Volmer current density (A cm^{-3})
m	Mass (kg)
Q	Heat transfer rate (W)
q	Discretization step
R	Universal gas constant (R = 8.3143) (J $mol^{-1}K^{-1}$)
r	Radial coordinate (cm)
R^{th}	Thermal conduction resistance (KW^{-1})
R_f	Film resistance on the electrodes surface (Ωcm^2)
R_s	Solid active material particle radius (cm)
T	Absolute Temperature (K)
t	Time (s)
t_0^+	Transference number of lithium ion
U	Equilibrium potential of an electrode
x	Cartesian coordinate (s)
T_b	Bottom Temperature (K)
T_c	Core Temperature (K)
T_h	Housing Temperature (K)
T_k	Cooler Temperature (K)
T_t	Terminal Temperature (K)
U_H	Enthalpy potential (V)

Greek symbols

α_a, α_c	Anodic and cathodic charge transfer coefficients
δ	Thickness (cm)
η	Surface overpotential of an electrode reaction (V)
κ	Electrolyte phase ionic conductivity ($\Omega^{-1}cm^{-1}$)
κ_D	Electrolyte phase diffusion conductivity ($\Omega^{-1}cm^{-1}$)
ϕ	Volume averaged electrical potential (V)
ρ	Density (kgm^{-3})
σ	Conductivity of solid active material ($\Omega^{-1}cm^{-1}$)
θ	Reference stoichiometry
ε_e	Electrolyte phase volume fraction
ε_s	Active material volume fraction

Table 10
Combined ECHTM model results - RMSE and MAE in the terminal voltage and the measured temperatures.

Symbol	Validation cycle	
	RSME	MAE
Terminal voltage [V]	0.039	0.025
$T_t[°C]$	0.415	0.343
$T_h[°C]$	0.673	0.555
$T_c[°C]$	0.493	0.404
$T_b[°C]$	1.134	0.927

Superscripts

eff	Effective
n	Anode
p	Cathode
sep	Separator
th	Thermal

Subscripts

∞	Volume average
amb	Ambient
conv	Generation
e	Electrolyte phase
gen	Generation
irr	Irreversible
mix	Mixing
ref	Reference
rev	Reversible
s	Solid phase
sr	Side reactions

References

[1] B. Schweighofer, K.M. Raab, G. Brasseur, Modeling of high power automotive batteries by the use of an automated test system, Instrumentation and Measurement, IEEE Trans. 52 (4) (2003) 1087–1091.

[2] M. Chen, G. Rincón-Mora, et al., Accurate electrical battery model capable of predicting runtime and iv performance, Energy conversion, IEEE Trans. 21 (2) (2006) 504–511.

[3] M.W. Verbrugge, R.S. Conell, Electrochemical and thermal characterization of battery modules commensurate with electric vehicle integration, J. Electrochem. Soc. 149 (1) (2002) A45–A53.

[4] M. Farag, M. Fleckenstein, S.R. Habibi, Li-ion battery SOC estimation using non-linear estimation strategies based on equivalent circuit models, in: SAE Technical Paper Series, SAE International, 2014.

[5] G.L. Plett, Extended kalman filtering for battery management systems of lipb-based hev battery packs: Part 1. background, J. Power Sources 134 (2) (2004) 252–261.

[6] G.L. Plett, Extended kalman filtering for battery management systems of lipb-based hev battery packs: Part 2. modeling and identification, J. Power Sources 134 (2) (2004) 262–276.

[7] G.L. Plett, Extended kalman filtering for battery management systems of lipb-based hev battery packs: Part 3. state and parameter estimation, J. Power Sources 134 (2) (2004) 277–292.

[8] M. Farag, S. Gadsden, S. Habibi, J. Tjong, A comparative study of li-ion battery models and nonlinear dual estimation strategies, in: 2012 IEEE Transportation Electrification Conference and Expo (ITEC), IEEE, 2012, pp. 1–8.

[9] V.R. Subramanian, V.D. Diwakar, D. Tapriyal, Efficient macro-micro scale coupled modeling of batteries, J. Electrochem. Soc. 152 (10) (2005) A2002–A2008.

[10] L. Cai, R.E. White, Reduction of model order based on proper orthogonal decomposition for lithium-ion battery simulations, J. Electrochem. Soc. 156 (3) (2009) A154–A161.

[11] J.C. Forman, S. Bashash, J.L. Stein, H.K. Fathy, Reduction of an electrochemistry-based li-ion battery model via quasi-linearization and padé approximation, J. Electrochem. Soc. 158 (2) (2011) A93–A101.

[12] M. Doyle, T.F. Fuller, J. Newman, Modeling of galvanostatic charge and discharge of the lithium/polymer/insertion cell, J. Electrochem. Soc. 140 (6) (1993) 1526–1533.

[13] T.F. Fuller, M. Doyle, J. Newman, Simulation and optimization of the dual lithium ion insertion cell, J. Electrochem. Soc. 141 (1) (1994) 1–10.

[14] C. Wang, W. Gu, B. Liaw, Micro-macroscopic coupled modeling of batteries and fuel cells i. model development, J. Electrochem. Soc. 145 (10) (1998) 3407–3417.

[15] K. Smith, C.D. Rahn, C.-Y. Wang, et al., Model-based electrochemical estimation and constraint management for pulse operation of lithium ion batteries, Control Systems Technology, IEEE Trans. 18 (3) (2010) 654–663.

[16] M. Golubitsky, I. Stewart, et al., Singularities and Groups in Bifurcation Theory, vol. 2, Springer Science & Business Media, 2012.

[17] B.S. Haran, B.N. Popov, R.E. White, Determination of the hydrogen diffusion coefficient in metal hydrides by impedance spectroscopy, J. Power Sources 75 (1) (1998) 56–63.

[18] S.K. Rahimian, S. Rayman, R.E. White, Extension of physics-based single particle model for higher charge–discharge rates, J. Power Sources 224 (2013) 180–194.

[19] D. D. Domenico, G. Fiengo, A. Stefanopoulou, Lithium-ion battery state of charge estimation with a kalman filter based on a electrochemical model, in: Control Applications, 2008. CCA 2008. IEEE International Conference on, IEEE, 2008, pp. 702–707.

[20] A. Smyshlyaev, M. Krstic, N. Chaturvedi, J. Ahmed, A. Kojic, PDE model for thermal dynamics of a large li-ion battery pack, in: Proceedings of the 2011 American Control Conference, IEEE, 2011, pp. 959–964.

[21] X. Hu, S. Asgari, S. Lin, S. Stanton, W. Lian, A linear parameter-varying model for hev/ev battery thermal modeling, in: 2012 IEEE Energy Conversion Congress and Exposition (ECCE), IEEE, 2012, pp. 1643–1649.

[22] G. Guo, B. Long, B. Cheng, S. Zhou, P. Xu, B. Cao, Three-dimensional thermal finite element modeling of lithium-ion battery in thermal abuse application, J. Power Sources 195 (8) (2010) 2393–2398.

[23] N. Baba, H. Yoshida, M. Nagaoka, C. Okuda, S. Kawauchi, Numerical simulation of thermal behavior of lithium-ion secondary batteries using the enhanced single particle model, J. Power Sources 252 (2014) 214–228.

[24] N. Damay, C. Forgez, M.-P. Bichat, G. Friedrich, Thermal modeling of large prismatic lifepo 4/graphite battery. coupled thermal and heat generation models for characterization and simulation, J. Power Sources 283 (2015) 37–45.

[25] C. Forgez, D.V. Do, G. Friedrich, M. Morcrette, C. Delacourt, Thermal modeling of a cylindrical lifepo 4/graphite lithium-ion battery, J. Power Sources 195 (9) (2010) 2961–2968.

[26] C. Lin, K. Chen, F. Sun, P. Tang, H. Zhao, Research on thermo-physical properties identification and thermal analysis of ev li-ion battery, in: 2009 IEEE Vehicle Power and Propulsion Conference, IEEE, 2009, pp. 1643–1648.

[27] H.E. Perez, J.B. Siegel, X. Lin, A.G. Stefanopoulou, Y. Ding, M.P. Castanier, Parameterization and validation of an integrated electro-thermal cylindrical lfp battery model, in: ASME 2012 5th Annual Dynamic Systems and Control Conference Joint with the JSME 2012 11th Motion and Vibration Conference, American Society of Mechanical Engineers, 2012, pp. 41–50.

[28] X. Lin, H.E. Perez, J.B. Siegel, A.G. Stefanopoulou, Y. Li, R.D. Anderson, Y. Ding, M.P. Castanier, Online parameterization of lumped thermal dynamics in cylindrical lithium ion batteries for core temperature estimation and health monitoring, IEEE Trans. Control Syst. Technol. 21 (5) (2013) 1745–1755.

[29] W. Shyy, Y.-C. Cho, W. Du, A. Gupta, C.-C. Tseng, A.M. Sastry, Surrogate-based modeling and dimension reduction techniques for multi-scale mechanics problems, Acta Mech. Sin. 27 (6) (2011) 845–865, http://dx.doi.org/10.1007/s10409-011-0522-0.

[30] Y.-B. Yi, A. Sastry, Analytical approximation of the percolation threshold for overlapping ellipsoids of revolution, in: Proceedings of the Royal Society of London A: Mathematical, Physical and Engineering Sciences, vol. 460, The Royal Society, 2004, pp. 2353–2380.

[31] Y.-B. Yi, C.-W. Wang, A.M. Sastry, Two-dimensional vs. three-dimensional clustering and percolation in fields of overlapping ellipsoids, J. Electrochem. Soc. 151 (8) (2004) A1292, http://dx.doi.org/10.1149/1.1769272.

[32] M. Farag, M. Fleckenstein, S. Habibi, Continuous piecewise-linear, reduced-order electrochemical model for lithium-ion batteries in real-time applications, J. Power Sources 342 (2017) 351–362.

[33] D. Di Domenico, A. Stefanopoulou, G. Fiengo, Lithium-ion battery state of charge and critical surface charge estimation using an electrochemical model-based extended kalman filter, J. Dyn. Syst. Meas. Control 132 (6) (2010) 061302.

[34] D. Bernardi, A general energy balance for battery systems, J. Electrochem. Soc. 132 (1) (1985) 5.

[35] Y. Kobayashi, N. Kihira, K. Takei, H. Miyashiro, K. Kumai, N. Terada, R. Ishikawa, Electrochemical and calorimetric approach to spinel lithium manganese oxide, J. Power Sources 81–82 (1999) 463–466.

[36] S.J. Bazinski, X. Wang, The influence of cell temperature on the entropic coefficient of a lithium iron phosphate (lfp) pouch cell, J. Electrochem. Soc. 161 (1) (2013) A168–A175.

[37] J.P. Schmidt, A. Weber, E. Ivers-Tiffée, A novel and precise measuring method for the entropy of lithium-ion cells, Electrochimica Acta 137 (2014) 311–319.

[38] K. Jalkanen, T. Aho, K. Vuorilehto, Entropy change effects on the thermal behavior of a lifepo4/graphite lithium-ion cell at different states of charge, J. Power Sources 243 (2013) 354–360.

[39] M. Dubarry, V. Svoboda, R. Hwu, B. Yann Liaw, Incremental capacity analysis and close-to-equilibrium ocv measurements to quantify capacity fade in commercial rechargeable lithium batteries, Electrochem. Solid-State Lett. 9 (10) (2006) A454.

[40] K. Kumaresan, G. Sikha, R.E. White, Thermal model for a li-ion cell, J. Electrochem. Soc. 155 (2) (2008) A164.

[41] S. Wang, Entropy and heat generation of lithium cells/batteries, Chin. Phys. B 25 (1) (2016) 010509.

[42] K.E. Thomas, J. Newman, Thermal modeling of porous insertion electrodes, J. Electrochem. Soc. 150 (2) (2003) A176.

[43] K.E. Thomas, J. Newman, Heats of mixing and of entropy in porous insertion electrodes, J. Power Sources 119 (2003) 844–849.

[44] Z. Li, J. Zhang, B. Wu, J. Huang, Z. Nie, Y. Sun, F. An, N. Wu, Examining temporal and spatial variations of internal temperature in large-format laminated battery with embedded thermocouples, J. Power Sources 241 (2013) 536–553.